

NUMERICAL AND EXPERIMENTAL STUDY OF THE AERODYNAMIC AND AEROELASTIC PERFORMANCE OF A LOW PRESSURE TURBINE

*Simonassi L., Benauer R. *, Zenz M., Leitl P. *, Heitmeir F., Marn A.*

Institute of Thermal Turbomachinery and Machine Dynamics, Graz University of Technology, Graz, Austria. Email: loris.simonassi@tugraz.at

* Bionic Surface Technologies GmbH, Graz, Austria

ABSTRACT

This work presents the results of an experimental and numerical investigation conducted in the framework of a project focused on the influence of inlet distortions on the aeroelastic and aerodynamic performance of a low pressure turbine.

The measurements were carried out in the subsonic test turbine facility at the Institute of Thermal Turbomachinery and Machine Dynamics at Graz University of Technology. Flow measurements were performed by means of five-hole-probe. In addition, a telemetry system in combination with strain gauges was applied to acquire the rotor blades vibration data.

The numerical investigation was carried out at Bionic Surface Technologies GmbH employing the commercial tool ANSYS CFX. Reynolds-Averaged Navier-Stokes (RANS) equations were used for solving the flow-field. For the flutter analysis, the modal shapes of the rotor blades were calculated by pre-stressed modal analysis in ANSYS Mechanical and the aeroelastic solution was computed for different Inter Blade Phase Angles (IBPA).

KEYWORDS

AEROELASTICITY, LOW PRESSURE TURBINES, FORCED RESPONSE, FLUTTER, CFD, STRAIN GAUGES.

NOMENCLATURE

Abbreviations

EF Eigenfrequency
EO Engine order
OP Operating point
SG Strain gauge
IGV Inlet guide vane
LPT Low pressure turbine
ND Nodal diameter

Greek

α Yaw angle
 γ Pitch angle

Symbols

Ma Mach number
P, Pt Static and Total Pressure
F Forcing function
 k Reduced Frequency
 C_{pt} Total pressure coefficient
M Mass
 v Absolute velocity

STTF-AAAI Subsonic Test Turbine Facility for Aerodynamic, Aeroelastic, Acoustic Investigations
TEGV Turbine exit guide vane
IBPA Interblade Phase Angle
TE Trailing Edge
TEC Turbine Exit Casing
SDOF Single Degree of Freedom System

ζ Damping
 ω, ω_n Angular and Natural frequency
 ρ Density
 w Relative velocity
Re Reynolds number
 C Viscous damping coefficient
 X, Y, H Excitation, response, transfer functions
 x, \dot{x}, \ddot{x} Displacement, speed, acceleration
 Y Frequency response function
K Spring constant
 c Chord

INTRODUCTION

Modern low pressure turbine (LPT) architectures of aero engines are designed in order to optimize components weight, decrease the fuel consumption and noise emissions. This can be achieved on one hand by the use of lighter materials or, on the other hand, by reducing the engine size. In particular, a widespread and effective solution is to decrease the axial distances between the blade rows and shorten the intermediate turbine duct, also known as turbine centre frame. As a consequence, it becomes increasingly important to investigate the influence of propagating circumferential distortions of total pressure and temperature, propagating from the combustion chamber or from the upstream stages, on the forced response and flutter of the turbine rotor blades.

To investigate such influences, a national funded research project was undertaken, with the partnership between the Institute of Thermal Turbomachinery and Machine Dynamics of Graz University of Technology and the Small Business Bionic Surface Technologies and Springer and Pieringer EDV OG. The objectives of this project are to perform aerodynamic and vibration measurements in a subsonic test turbine facility and to develop and validate a numerical tool for aeroelastic analysis of rotor bladings, in order to study the influence of inflow perturbations on the vibrations of an unshrouded LPT rotor of a modern aircraft engine.

However, several experimental tests in annular cascades focused on blade vibration already exist. For instance, measurements regarding the mode shape sensitivity of an oscillating low pressure turbine cascade were conducted by Nowinski and Panovsky (2000). Vogt and Fransson (2004), Kielb and Abhari (2003) analysed the blade vibratory response with and without aerodynamic loading. An overall summary of the most important design issues, effects and vibration characteristics was given by Srinivasan (1997). Recent studies conducted by Corral and Vega (2016-a, b) and (2017-a, b) have numerically verified the conclusions drawn by this author. Their studies presented as well a comprehensive theory to explain the impacts on blade flutter of mode-shape, aerodynamic loading, and the key aeroelastic design parameters.

Regarding forced response research in rotating turbine test rigs, only a few publications can be found in the open literature. Hennings and Elliott (2002) performed experiments on a single-stage high-pressure turbine and generated a dataset to validate and calibrate computational tools. Additionally, a study aimed to determine what is the impact of unsteady aerodynamic forces from partial admission onto the control stage rotor in a two-stage axial test turbine was carried out by Fridh et al. (2012).

Numerical methods for the prediction of flutter phenomena in turbomachinery are constantly increasing their complexity. Commonly, the separation between the structural and the aerodynamic evaluations allows the application of different solution methods. Transient flows can be resolved with the linear harmonic approach, assuming small perturbations around a mean steady value, as presented by Campobasso and Giles (2002), Hall et al. (2002) and McBean et al. (2002).

Previous forced response measurements were carried out in the subsonic test turbine facility of the Institute of Thermal Turbomachinery and Machine Dynamics of the Graz University of Technology, during a preceding research project. Specifically, the effect of different TEGV designs on the LPT rotor blade vibration was studied by Schönleitner et al. (2016-a), and Marn et al. (2016) analysed the influence of stator-rotor axial distance on the forced response of the rotor blading.

The present study succeeds the analysis of the previous researches, presenting both experimental and numerical results. The flow field, measured by means of five-holes-probe downstream of the LPT rotor blading, will be analysed and put in relation with the blade vibration data acquired with the strain gauges during steady and transient operations, on and off-resonance. Additionally, numerical simulations were employed to analyse the stability characteristic of the rotor blading in terms of aerodynamic damping for different interblade phase angles. The results of this investigation will be used to validate numerical tool for the aeroelastic analysis of rotor bladings which is currently under development.

EXPERIMENTAL INVESTIGATION

The details of the experimental investigation are discussed in this section. The experimental setup, the operating conditions and the measurement techniques for both the aerodynamic and vibration measurements are described. Then, the flow downstream of the LPT rotor and the results of the vibration measurements will be presented and analysed.

Test Facility

The cross section of the Subsonic-Test-Turbine-Facility for Aerodynamic, Aeroelastic and Acoustic Investigations located at the Institute of Thermal Turbomachinery and Machine Dynamic of the Graz University of Technology is depicted in Figure 1. The compressed air is supplied by a 3MW compressor station, the maximum pressure ratio is 2 and the maximum mass flow rate is 15 kg/s at a stage inlet temperature of 100°C. A de-swirler and a perforated metal plate are mounted upstream of the test section inlet in order to provide well-defined and uniform inflow conditions. The test turbine LPT stage, which is representative of the last stage of a commercial engine, consists of the inlet guide vanes (IGVs), the stator and the rotor. Downstream of the rotor a 360 deg rotatable aero-acoustic measurement section is located. Finally, the air leaves the rig through the exhaust casing of the facility. A full description of the test facility is given in Moser et al. (2007).

The aerodynamic design of the low pressure turbine stage was performed by MTU Aero Engines. The turbine diameter is approximately half of that of a commercial aero engine LPT. The studied set-up included a vane-less TEC mounted downstream of the LPT rotor in order to simplify the numerical evaluation and to avoid any influence of the TEGVs on the measurements. The blade and vane counts and the main geometrical details of the turbine are displayed in Table 1.

Operating Conditions

The results presented in this paper are referred to an operating point defined for aeroelastic purposes using the aero design point of the last stage LPT, derived from the scaling of current LPT design reduced speed, reduced mass flow (both referred to 288.15 K and 1013.25 mbar) and pressure ratio. Table 1 shows the reduced mass flow, the reduced speed, the pressure ratio and the inlet total temperature of the operating point at which the aerodynamic and aeroelastic investigation discussed in the paper has been carried out. The vibration measurements were conducted both at the nominal operating point presented above and additionally by gradually increasing or decreasing the rotor speed across a speed range varying from 90% to 125% of the nominal operating point speed at a sweep rate of approximately 5 rpm/s, while maintaining the nominal turbine pressure ratio constant. Furthermore, transient vibration measurements were performed also during start-up.

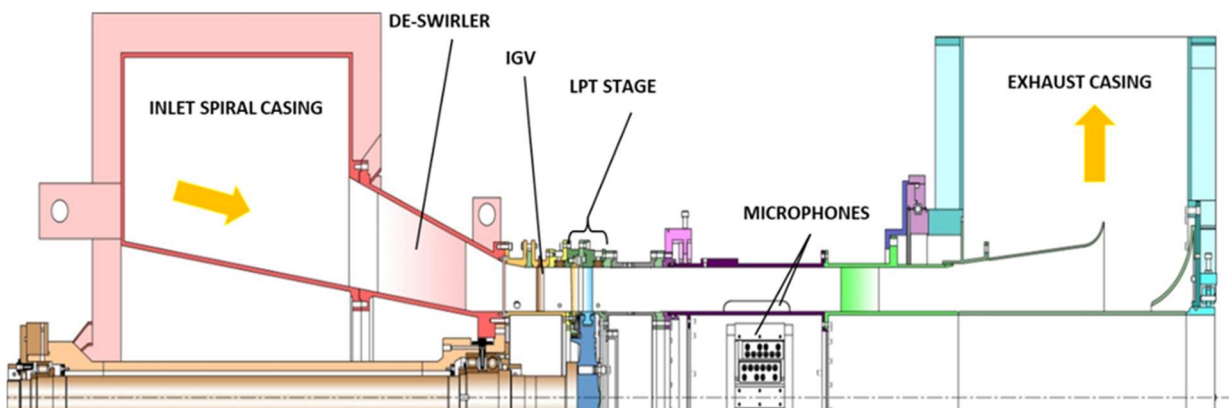


Figure 1: Cross section of the STTF – AAI. Measurement plane right downstream of the LPT rotor.

Table 1: Geometry details and operating conditions.

Geometry Details		Operating Conditions	
Number of Blades/Vanes			
IGV/Stator/Rotor	83/96/72	Stage pressure ratio	1.16
Vane-less TEC	-	Corrected speed	2999 rpm
Tip gap/Blade height	1%	Corrected mass flow	6.82 kg/s
Hub/Tip radii	2/3	Inlet total temperature	75.5 °C

Instrumentation

Flow measurements

As already mentioned, the aerodynamic measurements downstream of the LPT rotor were carried out by means of five-hole-probe. The probe has a head with a diameter of 2.5 mm. The calibration range is shown in Table 2, where negative values of the yaw angle indicate a counter-rotating flow and negative values of pitch angle indicate the flow pointing towards the hub. The correlation between the calibration characteristics and the value to be measured is given by a multi-parameter approximation.

The measurement plane is located downstream of the rotor trailing edge (TE) at a distance of 60% of the axial rotor blade chord length. The measured sector covers 8 stator pitches and about 95% of the span. Traversing was done along radial lines. At each measurement point the probe was rotated in the flow direction to reach the highest accuracy and to ensure to be within the calibration range.

Vibration measurements

The LPT rotor was instrumented with 12 strain gauges applied on different blades. The position of the strain gauges on the blades was discussed previously in Schönleitner et al. (2015) and Schönleitner et al. (2016-a). Figure 2 (a) shows a strain gauge applied on a rotor blade, while the position of the three sensors that will be discussed in details throughout this work is shown in Figure 2 (c). The strain gauges were employed in combination with a telemetry system able to operate at rotational speeds up to 11000 rpm and temperatures up to 150 °C and to acquire data at a maximum sample rate of 400 kSamples/s. The telemetry system is depicted in Figure 2 (b). During the measurements, the strain gauge signals were transmitted via antenna outside of the test rig where they were acquired using a National Instruments PXI chassis including two PXI 4498 Modules. This is a high-accuracy data acquisition module with a sampling rate of up to 204800 samples/s. The acquired data were then transmitted to a PC via fibre-optic cabling.

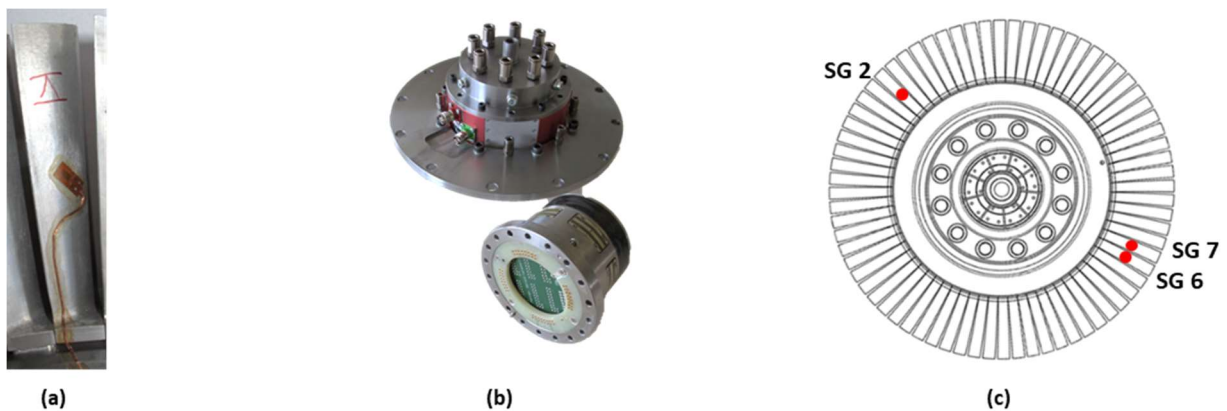


Figure 2: Details of the strain gauges measurement system. (a) Application of the strain gauge on one blade. (b) Telemetry system. (c) Position of the three strain gauges analysed in depth in this paper.

Table 2: Measurement uncertainties and calibration range of the five-hole-probe.

Measurement uncertainties				Calibration range			
Ma	+0.006	-0.003	[-]		Minimum	Maximum	Step
α	+0.5	-0.08	[deg]	Ma	0.1	0.8	0.1
Pt	+3.3	-3.0	[mbar]	α	-20	20	4
P	+5.3	-5.2	[mbar]	γ	-20	20	4

Measurements uncertainties

The pressure measurement system is constituted of 11 multichannel pressure transducers with an accuracy of 0.05%. The measurement uncertainties (within a 95% confidence interval) of the five-hole-probe measurements are shown in Table 2. These values are positive and negative deviations and contain the error due to the approximation, random error and the systematic error of the pressure transducers

Concerning the vibration measurements, the strain gauge resistance is $350\Omega \pm 0.30\%$ with a gauge factor of $2.05 \pm 1.0\%$, a transverse sensitivity of 0.0% and a temperature coefficient of gauge factor of $101 \pm 10 [10^{-6}/K]$. In addition, the signal amplifier of the telemetry system has a zero drift of $0.02\%/^{\circ}C$ and an accuracy of linearity of 0.1%.

During the test runs the variation of speed was maintained below 0.3% of the nominal operating speed, while the measurement uncertainty of the inlet temperature measurement is about $\pm 0.5 K$, which guarantees low fluctuations around the nominal inlet temperature. In general, the variation of the operating parameters (pressure ratio, corrected speed, speed, total pressure and temperature at rig inlet) between different measurement days was always below 0.2%.

Experimental Results

The following sections deal with the aerodynamic and aeroelastic results of the experimental investigation measurement. In particular, the circumferential distribution of the main flow quantities measured by means of five-hole-probe at the exit of the rotor will be analysed together with the results of the vibration measurements on the rotor blades. For the sake of brevity, the results obtained from the analysis of nine strain gauges will be presented, but only the data of three strain gauges is studied in details.

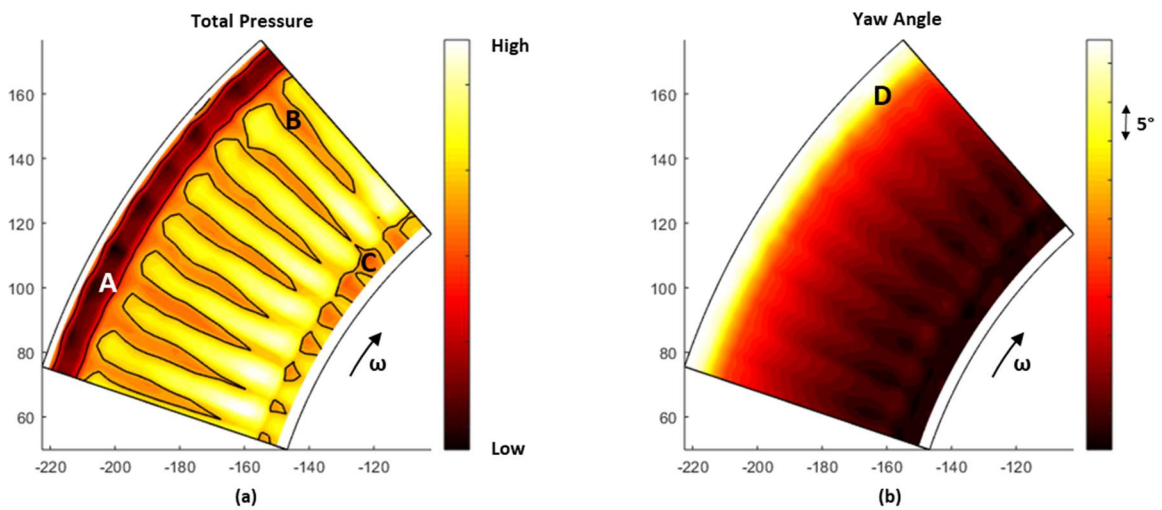


Figure 3: Flow field downstream of the LPT rotor measured by mean of five-holes-probe. (a) Total pressure and (b) Yaw angle.

Flow

Figure 3 shows aft-looking forward views of the circumferential distribution of total pressure (a), and yaw angle (b). As already stated by Marn et al. (2014), the rotor flow structures appear as circumferentially uniform bands that are modulated by the structures coming from the upstream stator and IGV rows.

Furthermore, some flow field distortions due to the secondary flows can be identified both at the hub and at the tip. Remarkably low total pressure is shown by the tip leakage vortex, (marked with A in Figure 3) at about 90% of the channel height. Additionally, the increase in yaw angle due to the effect of the tip leakage vortex can be observed also in Figure 3 (b), where it has been marked with letter D. In the lower passage region, the hub secondary vortices can be observed at approximately 15% of the span (marked with letter C in Figure 3). The effect of the uneven blade count and of the clocking between the inlet guide vanes and the stators can also be seen in the non-uniformity of these structures.

Moreover, the modulation due to the upstream stator wakes prevail in the region between 15% and 80% of the passage (B in Figure 3). To highlight the position of the stator flow structures it is possible to introduce a total pressure coefficient, defined in Equation 1, similarly to Lengani et al. (2012), as the nondimensional difference between the total pressure and its circumferential average:

$$C_{pt} = \frac{p_t - p_{t,AVE}}{1/2 \rho W_{AVE}^2} \quad (1)$$

Isocontour lines of the total pressure coefficient are superimposed to the total pressure plot of Figure 3 (a) and the areas enclosed inside correspond to a negative C_{pt} and match exactly with the number of the stator vanes present upstream. This allows us to directly identify the position of the structures produced by the stator row.

For the purpose of this study, the most important element that can be obtained from the analysis of the flow field downstream of the rotor is that the blades face different effects generated by the stator vanes upstream, which affect the rotor wakes, the rotor core flow and that can be directly linked to the excitation of the rotor blading (e.g. Marn et al. 2016). In particular, the flow structures originating from the stator vanes directly excite the rotor blades and represent the engine order EO96.

Moreover, according to the theory developed by Tyler and Sofrin (1962), the pressure patterns propagating downstream of a turbomachinery stage are restricted only to the ones generated by the interaction between blades and vanes. An example of the influence of these pressure patterns on blade vibration can be found in Marn et al. (2016) and Simonassi et al. (2018).

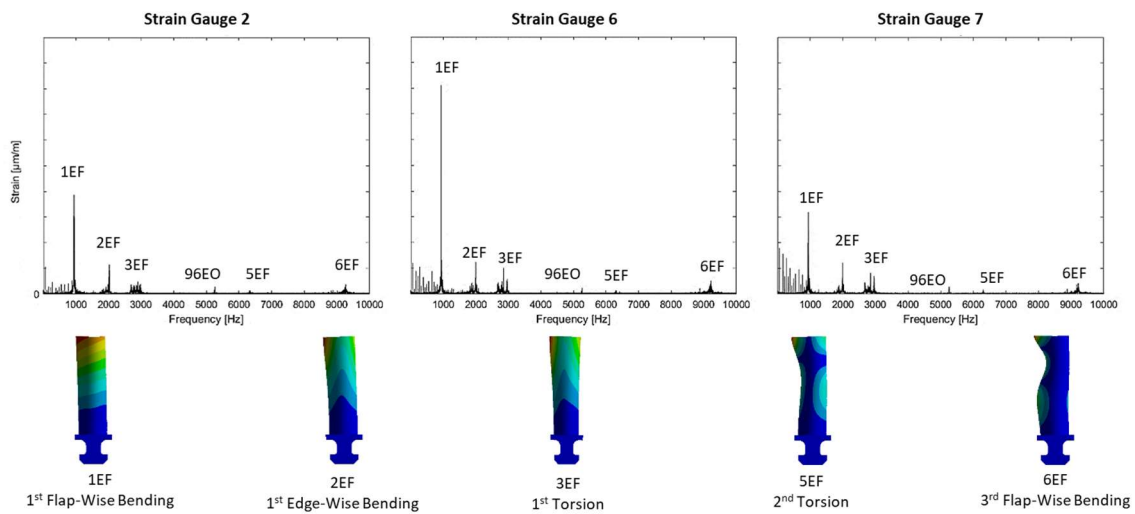


Figure 4: Forced response spectra of the three analysed strain gauges and corresponding depiction of the blade modes evaluated according to Schönleitner et al. (2015).

Vibrations

All time-resolved strain gauge data were averaged with respect to the rotational speed and then transferred to the frequency domain for further analysis. The spectra obtained have a resulting frequency resolution of 1 Hz.

Figure 4 displays the spectra of three strain gauges, allowing the identification of the characteristics of the main modes. The highest peak in all spectra is related to the first eigenfrequency (1st flap-wise bending mode) and is located around 930 Hz. The second eigenfrequency is at 1995 Hz and is the 1st edge-wise bending mode. The third peak in the spectra represents the 1st torsion mode at approximately 2850 Hz. Another peak can be observed at a frequency of 9220 Hz and corresponds to the 3rd flap-wise bending mode. At 5280 Hz it is possible to notice the response of the rotor blades to the forcing due to the excitation corresponding to the engine order 96, originated by the stator wakes. The amplitude related to the EO 96 is very low compared to the amplitude of the other peaks. This is due to the fact that the operating point chosen for this investigation is far from a condition of resonance, as demonstrated by the distance between the excitation due to the EO 96 and the eigenfrequencies. Since the amplitude of the fourth mode is small both in the spectra of Figure 4 and in the Campbell diagram of Figure 9, it was chosen to exclude it from the present analysis.

Comparing the three spectra plotted in Figure 4, one can notice that the amplitudes of the peaks are different, in particular concerning the peak corresponding to the 1st edge-wise bending mode. In fact, SG6 shows a higher amplitude than the other two strain gauges, while the SG2 has a smaller amplitude of the second eigenfrequency. Additionally, the strain gauge which shows the highest amplitude for the forced response related to the excitation of the EO 96 is SG1.

More details regarding the vibrations of the rotor blading can be obtained from the analysis of the sensors positioned on different blades around the rotor. The plots depicted in Figure 5 present the results of nine strain gauges. In particular, the distribution of the amplitudes of the main modes introduced above are shown in Figure 5 (a). The mode showing the maximum amplitude and the maximum scatter between the amplitudes measured by different strain gauges is the 1st eigenfrequency. SG6 gives the highest amplitude for the first eigenfrequency, while SG1 the lowest.

According to Srinivasan (1997), an uneven pattern of blade amplitudes, with many harmonics present in every mode, is normal for a real rotor. Manufacturing tolerances, material inhomogeneities and irregular mounting can cause mistuning, which breaks the harmonics of the traveling wave modes. It is therefore of great importance to know the behaviour of each single blade to correctly evaluate the individual forced response, as already observed by Henings and Elliott (2002). Additional information can be obtained analysing the eigenfrequencies and the response to the EO 96 of the nine instrumented blades illustrated in Figure 5 (b). The 6th and the 3rd modes show the highest deviation related to the average frequency. In general, the scatter of the eigenfrequencies measured with the strain gauges during the operation of the test rig at engine relevant operating conditions clearly demonstrates the influence of mistuning and matches the patterns obtained by Schönleitner et al. (2015) with a static shaker test.

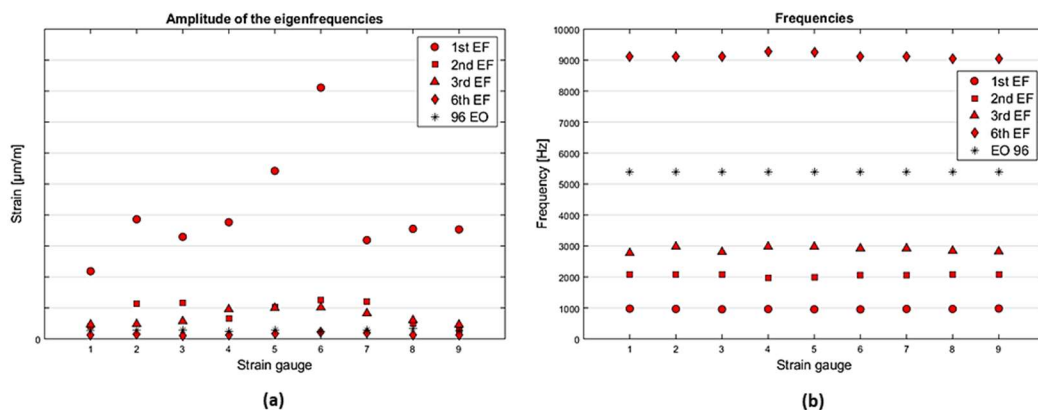


Figure 5: Amplitude and frequencies of nine strain gauges applied on nine different blades. Amplitude (a). Frequency (b).

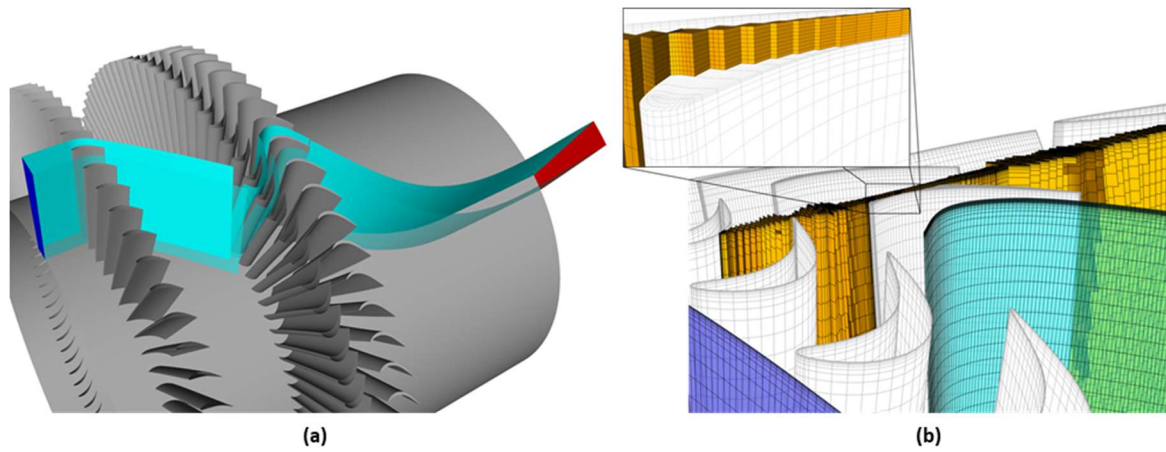


Figure 6: Overview of the mesh for the steady state calculation (a) and detailed view of the mesh in the tip gap region.

NUMERICAL INVESTIGATION

RANS Simulation

A steady-state Reynolds-averaged Navier-Stokes (RANS) simulation was performed with the aid of the commercial solver ANSYS® CFX® v19.0.

The investigated domain corresponds to the test-rig setup. In more details, as depicted in Figure 6 (a), it begins in front of the IGVs and ends downstream of the LPT rotor. The adopted numerical mesh is structured and consists of four cell zones and 580104 nodes. The Mixing Plane Method was used. As turbulence model, the $k-\omega$ SST model was chosen. As shown in Figure 6 (a), only a single periodic blade passage of each blade row was simulated, as the circumferential non-uniformities in the flow are averaged at the mixing plane interface. Moreover, the tip gap between rotor and casing was resolved; a detail of the mesh in the tip gap region is reported in Figure 6 (b).

The total and static pressure inlet and outlet boundary conditions were set in order to match the values measured upstream and downstream the LPT stage in the test-rig during the experimental campaign.

In order to assess the validity of the simulation, the radial distributions of circumferentially mass-averaged quantities evaluated numerically were compared with the measurements downstream of the LPT rotor. The results of this comparison can be seen in Figure 7, where the total pressure, yaw angle and Mach number are plotted. For the sake of clarity, the numerical results presented here are limited to the measurement sector in spanwise direction.

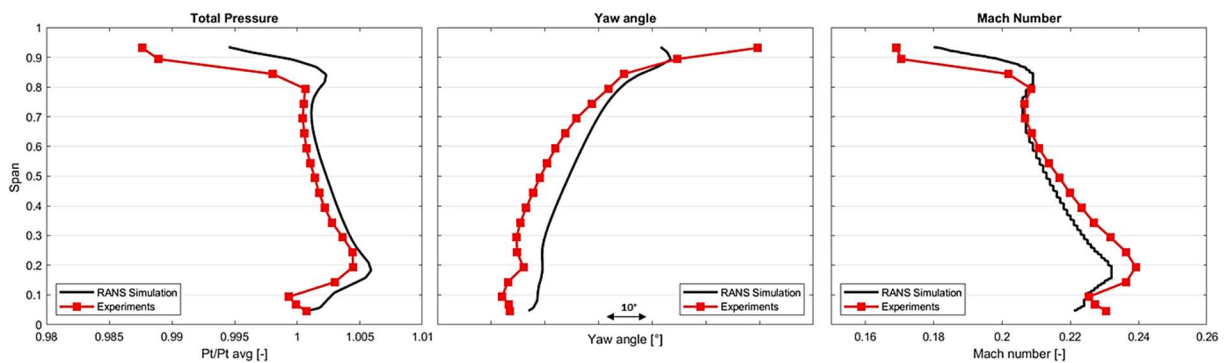


Figure 7: Comparison between the RANS simulations and the experimental results. Radial distributions of circumferentially mass averaged total pressure, yaw angle and Mach number.

The agreement between the computation and the measurements is good in the region between 20% and 80% span. A strong influence of the tip leakage vortex already highlighted in the description of the five-hole-probe results, can be noticed. In fact, at about 85% channel height both total pressure and Mach number experience a strong decrease while the yaw angle rapidly increases. In the simulation, the total pressure and Mach number drop resulting from the leakage flow results less marked than in the experimental data. The maximum yaw angle of the leakage flow is under predicted and close to the wall, the difference in yaw angle reaches its maximum value. Secondary flows can also be found near the hub region. Even though the overall trends are well predicted by the simulation, the comparison between the computation and the measurements shows a deviation of yaw angle as well as a higher total pressure and a lower Mach number at the hub. The differences between the experiments and the simulations can be attributed to the mixing plane setup. In fact, the effects of the stator and IGV wakes, which are present in the experiments, are not present in the simulations.

Flutter analysis

In order to obtain the mode shapes of the rotor blades, a pre-stressed modal analysis was done on one rotor blade, in which the pressure-loadings from the steady-state simulation and the rotational velocity were set as boundary conditions. Further, the blade was constraint in the root. An unstructured mesh consisting roughly of 440000 nodes was employed. The first three mode shapes evaluated with this modal analysis were successively utilised for the following blade-flutter analysis. The reduced frequencies for the calculated modes is 1.68 for the first flap-wise bending mode, 3.61 for the first edge-wise bending mode and 5.15 for the first torsion mode. The values are evaluated with the following equation:

$$k = \frac{\omega \cdot c}{v} \quad (2)$$

Once the boundary conditions and the mode shapes were established, it was then possible to solve the transient flow-field around the rotor blades using the Fourier methods implemented in ANSYS® CFX®. In more detail, the transient Harmonic Balance Method was used. Compared to the Time Integration Method, the Harmonic Balance Method solves only the final quasi-periodic flow state but not its evolution, providing the benefit of a much lower computational effort. To validate the accuracy of the Harmonic Balance Method, a comparison with a reference case evaluated using the Time Integration Method was done. The resulting difference between the aerodynamic damping coefficients evaluated with the two methods is 0.7%.

The domain employed for the flutter analysis simulation consists only of two rotor blades. In more details, the meshes around the two blades are connected with the required sampling interface for the Fourier methods. The boundary conditions were taken from the steady-state solution. At the inlet, the circumferentially mass-averaged velocity, the inflow angle and the total temperature were set as boundary conditions, while circumferential averaged static pressure was set at the outlet. In order to obtain information on the stability of the blade vibration, the three eigenfrequencies were investigated for different inter blade phase angles. Phase-shifted boundary conditions are used in the periodic boundaries to simulate the different IBPAs.

To evaluate the aeroelastic stability of a blade, the energy method is the most commonly used technique. In more details, the blade motion is unstable if the energy input from the surrounding flow is positive during a cycle of vibration. In order to apply this method, it is useful to evaluate the non-dimensional parameter aerodynamic damping, which directly indicates the energy exchange between the oscillating blade and its surrounding flow. Figure 8 shows the aerodynamic damping evaluated for different interblade phase angles and for the first (Figure 8 (a)), second (Figure 8 (b)) and third (Figure 8 (c)) eigenfrequencies.

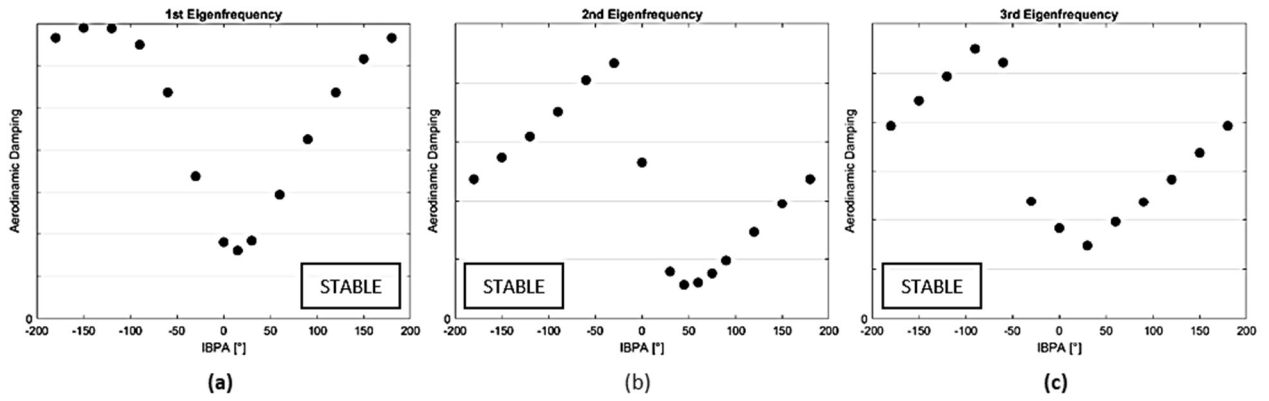


Figure 8: Aerodynamic damping coefficient of the first three eigenfrequencies. 1st flap-wise bending mode (a). 1st edge-wise bending mode (b). 1st torsion mode (c).

The shape of the curves depicted in the plots in Figure 8 is characteristic for the aerodynamic damping curves of turbomachinery blades. In particular, since the reduced frequency of the first mode falls within the frequency range investigated by Vega and Corral (2016-b), the shape of the aerodynamic damping as a function of the IBPA can be compared. It appears that the curve follows the same sinusoidal shape as the curves presented by Vega and Corral (2016-b) for $1 < k < 3$.

Observing the plots in more detail, it is possible to conclude that for all the studied eigenfrequencies, at the investigated operating point, the system is stable for every IBPA, as the aerodynamic damping is always positive. For the flap-wise bending mode, the vibrations become less stable close to IBPA = 0 deg and the lowest damping is reached for IBPA = 15 deg. A comparison between the two curves in Figure 8 (b) and (c) indicates a similar behaviour of the two modes at the variation of the IBPA, except for the fact that the torsion mode is overall more stable than the edge-wise bending mode, and that the 3rd eigenfrequency shows his lowest damping value for IBPA = 30 deg, whereas the 2nd eigenfrequency for IBPA = 45 deg.

COMPARISON BETWEEN EXPERIMENTAL AND NUMERICAL RESULTS

Forced response during transient operations

In order to better evaluate the validity of the stability predicted by the simulations, sweeps around the operating speed, across a speed range from 3100 rpm to 4100 rpm at constant pressure ratio were performed during simultaneous strain gauges' measurements. The response of the sensors across the operating range can be illustrated in a Campbell Diagram, where horizontal lines denote the blade and disk eigenfrequencies lines originating from the origin and proportional to the rotation frequency represent excitation lines (EO excitation). Additionally, the crossings between eigenfrequencies and excitation lines imply potential resonances.

Figure 9 shows the results of the measurements during transient operation (run-down) of the machine around the operating point. Observing the Campbell diagram of SG2 is depicted in Figure 9 (a) it is possible to identify the eigenfrequencies already described in the section regarding the strain gauges measurements. In addition, the excitation due to the stator vanes is clearly detectable and is denoted in the figure as EO96 and the fact that no crossing between the eigenfrequencies and the excitation line occurs, demonstrates that no possible resonances can arise around the operating point. Contrarily, the excitation due to the IGVs is not clearly noticeable in the Campbell diagram of Figure 9 (a), as its amplitude results too small for the visualisation.

Furthermore, During the velocity sweep no evidence of unstable vibration was recorded. This is visible in Figure 9 (b), where the signal of SG2, band pass filtered around the three investigated eigenfrequencies, is plotted (in red) over the nondimensional sweep time.

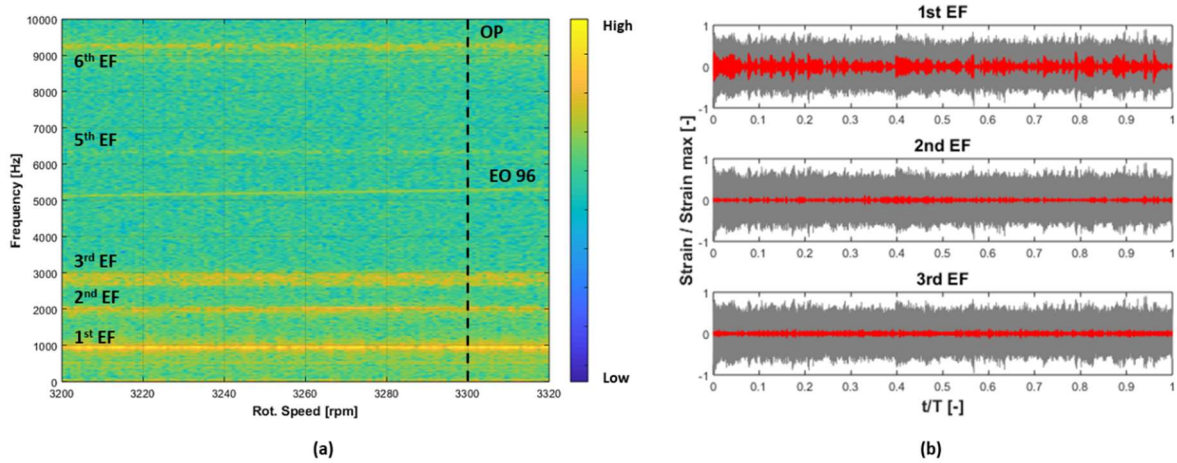


Figure 9: Campbell Diagram of strain gauge 2 (a) and vibration signature of the first three eigenfrequencies during sweep between 3200 rpm and 3320 rpm. (Grey: total signal of the strain gauge over time; Red: signal of the modes over time)

Contrarily to what was observed by Holzinger et al. (2015), none of the modes show the onset of self-excited blade vibrations with an exponential growth in amplitude, which would be caused by an overrun of the aeroelastic stability limit. Therefore, since the predicted damping coefficients are always positive for every IBPA, it can be assumed that the results of the numerical analysis on the vibrations of the rotor blades lead to the same conclusion as the data acquired during the test-rig experiments, as the amplitudes of the vibrations measured with the strain gauges show that the blades are stable during the operation around the investigated operating condition.

In order to obtain a more detailed assessment of the results of the numerical analysis, in the next section the predicted aerodynamic damping is compared with structural and total damping obtained experimentally.

Experimental evaluation of damping

During the start-up of the machine, crossings between the aerodynamic excitation due to the EO96 and the first three modes occur. Figure 10, shows a schematic Campbell diagram obtained for the speed range and the frequency spectrum of interest. Similarly to what was described in the previous section, the signals of the strain gauges were acquired during the resonance crossings, allowing the evaluation of the damping of the system. For the duration of the measurements, slow changes of the rotational speed allowed the blades to be excited by a forcing function of slowly changing frequency.

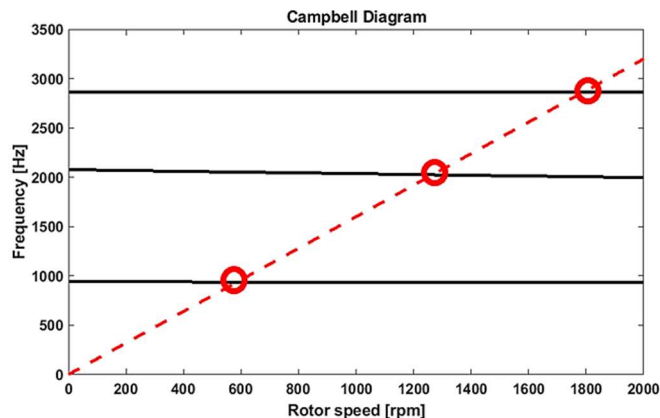


Figure 10: Campbell Diagram representing the resonance crossings between the EO96 and the first three eigenfrequencies during transient operation of the machine.

In turbomachinery, damping is composed by three main factors: structural damping, material damping and aerodynamic damping. Structural damping accounts for the energy dissipated during contacts between parts and its magnitude directly depends on the geometry and pressure of the contacts between components. Material damping instead is a characteristic of the material which represents the dissipation of energy during cyclic strain. Because significantly smaller than the other two contributors, it is typically ignored. Finally, aerodynamic damping characterises the dissipation due to the relative motion between the blade and the fluid.

According to Kammerer and Abbhari (2009), single degree of freedom systems (SDOF) can be used to characterise the blade vibration during transient operations. Therefore, throughout this study, damping will be evaluated similarly to the viscous damping of a vibrating SDOF. The problem is described by the following second order differential equation:

$$M\ddot{x} + C\dot{x} + Kx = F(t) \quad (3)$$

In the frequency domain, the transfer function that relates the response of the system to the excitation is given by:

$$H(\omega) = \frac{Y(\omega)}{X(\omega)} \quad (4)$$

In which $Y(\omega)$ denotes the response function and $X(\omega)$ the excitation function, which is assumed to be constant for the current application. In fact, the direct evaluation of the excitation measurement of the unsteady pressure on the rotor blades would otherwise be necessary. Consequently, the response amplitude can be evaluated as:

$$|H(\omega)|^2 = \frac{1/K^2}{\left[1 - (\omega/\omega_n)^2\right]^2 + [2\zeta(\omega/\omega_n)]^2} \quad (5)$$

Thus, the data measured during the sweeps through the resonance crossing can be fitted evaluating the parameters K , ω/ω_n and the total damping ratio ζ . A least square fit method was used to minimize difference between the curve fit and the measured resonant response.

The resonant response of the first, second and third eigenfrequency acquired during the resonance crossing are shown in Figure 11, together with the results of the curve-fitting. The data was non-dimensionalised with respect to the maximum spectral density of each case. A potential problem in the application of the curve-fit procedure is the presence in the considered band width of other maxima at frequencies different than the eigenfrequency main peak. However, in the all the three studied case, no other maxima can be identified in the frequency ranges of interest and consequently the data fitting shown in Figure 11 appears to correctly capture the shape of the resonance peak.

The damping ζ_{tot} evaluated with the curve-fit is shown in Table 3 for the three investigated eigenfrequencies. Together with the total damping, Table 3 contains also the structural damping ζ_s evaluated during a previous test campaign presented in Schönleitner et al. (2015) for the considered blade. The structural damping was obtained at room conditions and at standstill by means of shaker excitation and laser vibrometer measurements. It is necessary to consider that the mechanical damping was obtained at rest, therefore it is expected that during operation it will be influenced by the centrifugal forces due to the rotation. Additionally, the average value of the aerodynamic damping obtained with the numerical flutter analysis is included in the table as well as the predicted variation over the IBPA.

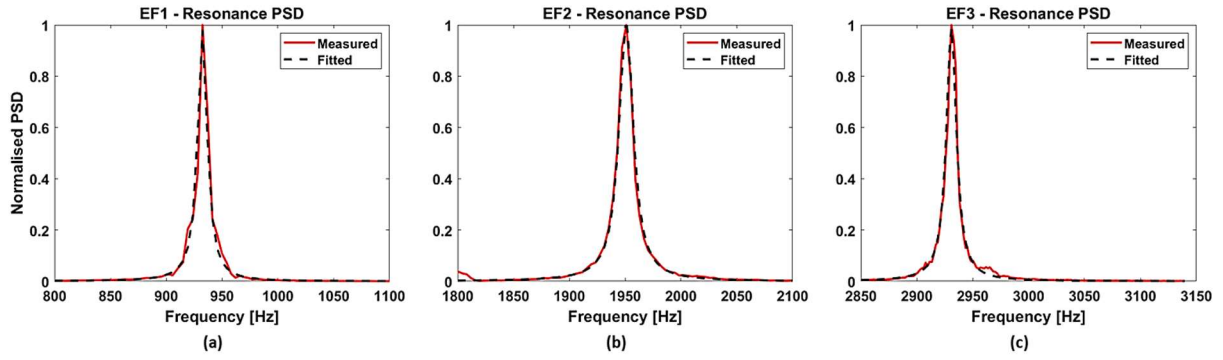


Figure 11: Resonant response of mode 1 (a), mode 2 (b) and mode 3 (c), measured and fitted for SG7.

Table 3: Damping evaluated from measurement data and predicted numerically.

Damping (e-4)				
Mode	ζ_{tot}	ζ_s	$\bar{\zeta}_A$ simulations	ζ_A variation
EF 1	51	18	23	13
EF 2	36	20	10	9
EF 3	19	25	33	20

A comparison between the predicted aerodynamic damping and the results of experimental evaluation can be made, similarly to Mischo et al (2018). Considering that the structural damping is expected to decrease with the rotational speed (Kielb and Abhari (2003)) and considering the difference between the structural damping and the total damping evaluated from the experimental data, an approximation of the aerodynamic damping can be obtained for the three eigenfrequencies. For the first two modes, the average aerodynamic damping predicted numerically compares well with the results of the experimental investigation. Concerning the third eigenfrequency, the predicted aerodynamic damping seems to be overestimated. This difference can be caused on one hand by the effect of the rotational speed on the measured damping and on the other hand by the steady state numerical method used for the simulations.

In general, this indicates that the Harmonic Balance Method used to solve the unsteady flow field around the rotor blades, from which the aerodynamic work and damping are derived, gives a reasonably accurate result for the first two modes. In fact, the numerically evaluated aerodynamic damping is of the same order of magnitude as the damping extrapolated from the measured data. However, this comparison can only be considered on a qualitative level, as more research is needed to understand the influence of the nodal diameter and of the rotational speed on the damping obtained experimentally. Furthermore, a transient analysis is necessary to study the effects of the wakes generated by the upstream vanes. Ultimately, the main outcome of this comparison is that both the numerical and the experimental aerodynamic damping lead to the conclusion that the rotor blades vibrations are stable.

CONCLUSIONS

Aerodynamic and vibration measurements have been carried out in a 1.5 low pressure test turbine stage, operated under engine relevant conditions, by means of five-hole-probe and strain gauges respectively.

The aerodynamic measurements were used to recognise the features that characterise the flow field downstream of the rotor. In particular, the tip leakage vortices, hub secondary vortices and the traces of wakes originated from the stator vanes were observed. Further, the stator wakes were identified as the main cause of aerodynamic excitation of the rotor blades.

Concerning the rotor vibrations, forced response measurements were performed by means of strain gauges applied on the blades, in combination with a telemetry system. The blades response was acquired both at the nominal operating point and during speed ramps across a rotational velocity range which included the nominal operating point as well as the resonant crossing of the first three eigenfrequencies. Five modes could be clearly observed with the first eigenfrequency dominating the forced response spectrum. Successively, a curve-fit procedure with the response of a SDOF model was applied with the aim to determine the critical damping ratio.

A numerical study was performed in order to evaluate the stability of the vibrations of the rotor blades at the investigated operating point. The CFD steady state simulations compared well with the aerodynamic experimental data. A qualitative comparison with the damping obtained from the measured data showed that the prediction provides a reasonably good result and that the blade vibration stability is predicted correctly. As an outlook to this work, further investigations including a transient numerical analysis to capture the effects of the wakes generated by the upstream vanes, as well as additional measurement aimed at understanding the influence of the nodal diameter and of the rotational speed on the damping are necessary. Furthermore, the results of this study will be used for the validation of a numerical tool for the aeroelastic analysis of rotor bladings which is currently under development.

ACKNOWLEDGEMENTS

The authors would like to thank Dr.techn. H.P. Pirker for operating the compressor station and his support and discussions during all experimental investigations.

This work has been carried out in the framework of the national funded TAKE-OFF programme within the research project EisenerZ (contract no. 855228) regarding the influence of inflow inhomogeneity on the vibration excitation of an LPT of a modern aircraft engine at the Institute for Thermal Turbomachinery and Machine Dynamics of the Graz University of Technology. The authors thank the Austrian Research Promotion Agency (FFG) and the Austrian Ministry for Transport Innovation and Technology (bmvit) for funding this project.

REFERENCES

- Nowinski, M., Panovsky, J., (2000). *Flutter Mechanism in Low Pressure Turbine Blades*. Journal of Engineering for Gas Turbine and Power, Vol. 122, pp. 82-88, January 2000.
- Vogt, D., Fransson, T. H., (2004). Experimental Investigation of Mode Shape Sensivity of an Oscillating Low Pressure Turbine Cascade at Design and Off-Design Conditions. Journal of Engineering for Gas Turbines and Power, Vol. 129, pp. 530-541, April 2004.
- Kielb, J. J., Abhari, R. S., (2003). *Experimental Study of Aerodynamic and Structural Damping in a Full-Scale Rotating Turbine*. Journal of Engineering for Gas Turbines and Power, 2003, Vol. 1025, pp. 102 -112, January 2003.
- Srinivasan, A., (1997). *Flutter and Resonant Vibration Characteristics of Engine Blades*. Journal of Engineering for Gas Turbines and Power, Vol. 119, pp. 741 -775, October 1997.
- Corral, R. and Vega, A., (2016-a). *The Low Reduced Frequency Limit of Vibrating Airfoils - Part I: Theoretical Analysis*. ASME Journal of Turbomachinery, Vol. 138, No. 2, February 2016, pp. 021004.
- Vega, A. and Corral, R., (2016-b). *The Low Reduced Frequency Limit of Vibrating Airfoils - Part II: Numerical Experiments*. ASME Journal of Turbomachinery, Vol. 128, No. 2, February 2016, pp. 021005.
- Corral, R. and Vega, A., (2017-a). Quantification of the Influence of Unsteady Aerodynamic Loading on the Damping Characteristics of Airfoils Oscillating at Low Reduced Frequency. Part I: Theoretical Support. ASME Journal of Turbomachinery, Vol 139, No. 3, pp 031010.
- Vega, A. and Corral, R., (2017-b). Quantification of the Influence of Unsteady Aerodynamic Loading on the Damping Characteristics of Airfoils Oscillating at Low Reduced Frequency. Part II: Numerical Verification. ASME Journal of Turbomachinery, Vol 139, No. 3, pp 031009.

- Hennings, H., Elliot, R., (2002). *Forced Response Experiments in a High Pressure Turbine Stage*. Proceedings of the ASME Turbo Expo, 2002, ASME Paper GT-2002-30453.
- Fridh, J., Laumert, B., Fransson, T., (2012). *Forced Response in Axial Turbines Under the Influence of Partial Admission*. Proceedings of the ASME Turbo Expo 2012. ASME Paper GT2012-68303.
- Hall, K. C., Thomas, J. P., Clark, W. S., (2002). *Computation of Unsteady Nonlinear Flows in Cascades Using a Harmonic Balance Technique*. AIAA Journal, Vol. 40, No. 5, May 2002, pp. 879–886.
- Campobasso, M. S., Giles, M. B., (2002). *Effects of Flow Instabilities on the Linear Analysis of Turbomachinery Aeroelasticity*. 38th AIAA/ASME/SAE/ASEE Joint Propulsion Conference & Exhibit, 2002. Indianapolis, IN.
- McBean, I., Liu, F., Hourigan, K., Thompson, M., (2002). *Simulations of Aeroelasticity in an Annular Cascade Using a Parallel 3-Dimensional Navier-Stokes Solver*. Proceedings of the ASME Turbo Expo 2002. ASME Paper GT2002-30366.
- Schönleitner, F., Selic, T., Schitter, C., Heitmeir, F., Marn, A., (2016-a). *Experimental Investigation of the Upstream Effect of Different Low Pressure Turbine Exit Guide Vane Designs on Rotor Blade Vibration*. Proceedings of the ASME Turbo Expo 2016. ASME Paper-No. GT2016-56067.
- Marn, A., Schönleitner, F., Mayr, M., Selic, T., Heitmeir, F., (2016). *On the Effect of Axial Spacing Between Rotor and Stator onto the Blade Vibrations of a Low Pressure Turbine Stage at Engine Relevant Operating Conditions*. Proceedings of the ASME Turbo Expo 2016. ASME Paper-No. GT2016-56069.
- Moser M, Kahl G, Kulhanek G, Heitmeir F., (2007). *Construction of a subsonic test turbine facility for experimental investigations of sound generation and propagation for low pressure turbines*. ISABE conference Beijing, Paper No. ISABE-2007-1366.
- Schönleitner, F., Traussnig, L., Marn, A., Heitmeir, F., (2015). *Modal Characterization, Strain Gauge Setup and 1-Way FSI of a Low Pressure Turbine Rotor Blading*. Proceedings of the ASME Turbo Expo 2015. ASME Paper GT2015-42717.
- Marn, A., Selic, T., Schönleitner, F., Heitmeir, F., Broszat, D., (2014). *Comparison of the Aerodynamics of Acoustically Designed EGVs and a State-of-the-Art EGV*. Proceedings of the ASME Turbo Expo 2014. ASME Paper GT2014-26090.
- Tyler, J.M., Sofrin, T.G., (1962). *Axial flow compressor noise studies*, SAE Transaction, Vol. 70, pp.309-332.
- Simonassi, L., Zenz, M., Zerobin, S., Heitmeir, F., Marn, A., Selic, T., (2018). *On the Influence of an Acoustically Optimized Turbine Exit Casing onto the Unsteady Flow Field Downstream of a Low Pressure Turbine Rotor*. Proceedings of the ASME Turbo Expo 2018. ASME paper GT2018-76725.
- Srinivasan, A, (1997). *Flutter and Resonant Vibration Characteristics of Engine Blades*. Journal of Engineering for Gas Turbines and Power, Vol. 119, pp. 741 -775.
- Lengani, D., Paradiso, B., Marn, A., Göttlich, E., (2012). *Identification of Spinning Mode in the Unsteady Flow Field of a Low Pressure Turbine*. Journal of Turbomachinery, Vol. 134, 2012.
- Holzinger, F., Wartzek, F., Schiffer, H. P., Leichtfuss, S., Nestle, M., (2016). *Self-Excited Blade Vibration Experimentally Investigated in Transonic Compressors: Rotating Instabilities and Flutter*. Proceedings of the ASME Turbo Expo 2015. ASME paper GT2015-43628.
- Kammerer, A., Abbhari, R. S., (2009). *Experimental Study on Impeller Blade Vibration During Resonance - Part I: Blade Vibration During Resonance Due to Inlet Flow Distortion*. Journal of Engineering for Gas Turbines and Power, vol. 131, pp. 1-11, 2009.
- Misco, B., Jenny, P., Mauri, S., Bidaut, Y., Kramer, M., Spengler, S., (2018). *Numerical and Experimental FSI Study to Determine Mechanical Stresses Induced by Rotating stall in Unshrouded Centrifugal Compressor Impellers*. Proceedings of the ASME Turbo Expo 2018. ASME paper GT2018-76344.